CMS Physics Analysis Summary

Contact: cms-pag-conveners-higgs@cern.ch 2016/03/15

Model independent search for Higgs boson pair production in the $b\bar{b}\tau^+\tau^-$ final state

The CMS Collaboration

Abstract

Results of a search for the production of Higgs boson pairs are presented. In this search one Higgs boson decays to a pair of b-quarks, and the other Higgs boson decays to a tau lepton pair where the tau leptons decay hadronically. The search is based on proton-proton collision data recorded by the CMS experiment at $\sqrt{s} = 8$ TeV in 2012, corresponding to an integrated luminosity of 18.3 fb^{-1}. The resonant and the non-resonant productions of Higgs boson pairs are studied. No significant excess with respect to the background-only hypothesis is observed in the data and therefore corresponding upper limits on cross section times branching ratio are set. In the case of resonant HH boson production, the limit on $\sigma(pp \to X) \times BR(X \to HH)$ for a resonance of spin 0 (spin 2) and mass m_X, ranges from 5.42 pb (3.97 pb) at $m_X = 300$ GeV to 0.14 pb (0.14 pb) at $m_X = 1000$ GeV. The limit on non-resonant production amounts to approximately 50 times the rate predicted by the SM.

1 Introduction

The discovery of a Standard Model (SM)-like Higgs boson [1, 2] encourages us to further probe the nature of electroweak symmetry breaking. The measurement of the Higgs self-coupling allows one to probe higher order terms in the Higgs potential, thereby providing valuable information concerning the mechanism responsible for electroweak symmetry breaking.

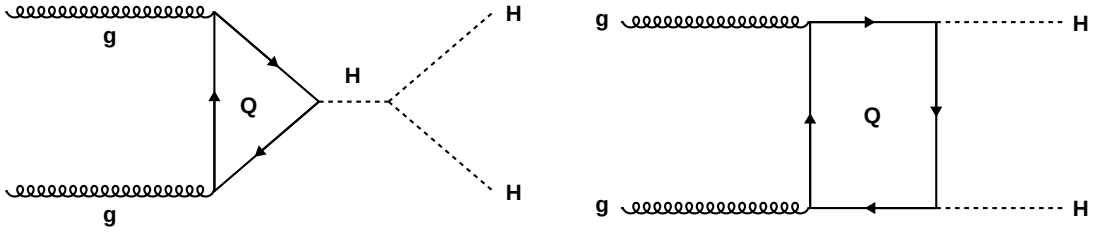

Figure 1: Leading-order diagrams for the production of a Higgs boson pair within the SM. The diagram on the left is sensitive to the trilinear Higgs boson self-coupling. The box diagram on the right interferes destructively with it, thus reducing the sensitivity.

Within the SM, the Higgs potential is given by:

$$V = \frac{1}{2}m_{\mathrm{H}}^2\Phi_{\mathrm{H}}^2 + \lambda v\Phi_{\mathrm{H}}^3 + \frac{\tilde{\lambda}}{4}\Phi_{\mathrm{H}}^4,$$

with $m_{\mathrm{H}} = 125$ GeV and $v = 246$ GeV [3]. The trilinear Higgs boson self-coupling can be measured, via di-Higgs production, at the LHC [4–8]. The leading order Feynman diagrams for SM di-Higgs production are shown in Fig. 1. The triangle diagram provides the sensitivity to the Higgs self-coupling and interferes destructively with the box diagram, resulting in the cross section for HH production to be small in the SM, amounting to 11.18 ± 0.56 (scale) $\pm$ 0.35 (PDF) $\pm$ 0.29 (α_s) fb at a center-of-mass energy of $\sqrt{s} = 8$ TeV [9]. This value has been computed at next-to-next-to-leading order (NNLO) precision, with next-to-next-to-leading logarithm (NNLL) corrections included. The scale uncertainty represents the unknown effect of higher order terms. The uncertainty arising due to the uncertainties on the parton distribution functions (PDF) have been computed following the recommendations given in [10] and using the PDF4LHC15NNLOMC set of PDF. An additional uncertainty of the order of 10% arises due to unknown top quark mass effects [11]. The mass distributions of the Higgs boson pair as expected in the SM and also for other values of λ exhibit a broad maximum around 400 GeV and varies as a function of λ. We refer to this case as *non-resonant* production.

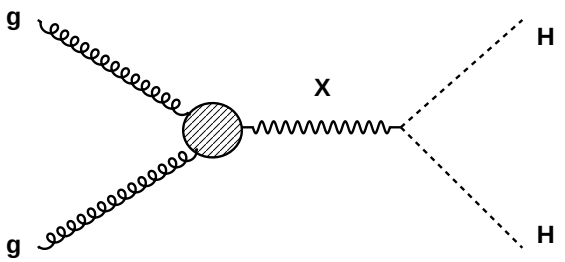

Figure 2: Leading-order diagram for the production of a pair of SM-like Higgs bosons of mass $m_{\mathrm{H}} = 125$ GeV, resulting from the decay of a new heavy resonance X.

The HH production rate may be enhanced if a heavy resonance X decays into a pair of Higgs bosons. Various theories beyond the SM postulate such decays, in particular: two-Higgs dou-

blet models [12, 13], composite Higgs models [14, 15], Higgs portal models [16, 17], and models inspired by warped extra dimensions [18]. In the latter theory, the heavy resonance X may either be a radion with spin 0 [19–22] or the first Kaluza-Klein (KK) excitation of the graviton with spin 2 [23, 24]. In case the heavy resonance has narrow width, a peak is expected in the HH mass distribution. We refer to this case as the *resonant* HH boson production.

Searches for HH production have been performed earlier by the ATLAS [25–27] and CMS Collaborations [28–30] in di-photon, multilepton and bb final states. This report presents the results of a search for the resonant as well as the non-resonant di-Higgs production with one of the Higgs bosons decaying to two bottom quarks, and the other decaying to two tau leptons where the tau leptons decay hadronically (τ_h). This decay channel has higher cross section than other channels and is also reasonably free from backgrounds. A search for a heavy resonance decaying to two tau leptons, and two b jets through a pair of 125 GeV Higgs bosons, has been previously performed by CMS and interpreted in the context of two-Higgs-doublet models and supersymmetric SM extensions [30]. This work extends that search to a larger resonance mass range in the theoretical contexts described above. The ATLAS collaboration has also searched for non-resonant and resonant di-Higgs boson production in the $b\bar{b}\tau\tau$ decay channel. They have observed (expected) a limit of 160 (130) times the SM cross section in the non-resonant case and observed (expected) a limit of 1.0 pb (0.66 pb) in the resonant case [27].

2 Datasets and Monte Carlo samples

This search is based on proton-proton collision data corresponding to an integrated luminosity of 18.3 fb^{-1} recorded at $\sqrt{s} = 8$ TeV center-of-mass energy in 2012. Signal samples for both the resonant and the non-resonant di-Higgs production, have been generated with MADGRAPH [31]. Signal samples for resonant HH production have been generated for both the spin 0 (radion) and the spin 2 (graviton) hypotheses of the X resonance at the $m_X = 300$, 500, 700 and 1000 GeV mass points. Shape templates for the signal extraction described in Sec. 8 are produced for intermediate mass points using the "horizontal template morphing" technique [32]. Signal shape templates for spin 0 and spin 2 resonances are produced in the range 300 to 1000 GeV in steps of 10 GeV. The efficiency and acceptance are interpolated linearly between the masses m_X = 300, 500, 700 and 1000 GeV.

Backgrounds arising from $Z/\gamma^* \to ee$, $Z/\gamma^* \to \mu\mu$, W+jets, $t\bar{t}$, single top, and di-boson (WW, WZ, ZZ) productions are modeled using Monte Carlo simulation. The $Z/\gamma^* \to \ell\ell$ (ℓ = e, μ), W+jets, $t\bar{t}$, and di-boson samples are generated with MADGRAPH, and the single top samples with POWHEG. Samples binned in parton level multiplicity are used for the $Z/\gamma^* \to \ell\ell$ and W+jets backgrounds, in order to enhance the background event statistics in regions of high signal purity. Hadronic shower and hadronization processes are modeled using PYTHIA6.4 [33]. Taus are decayed by TAUOLA [34]. Generated $Z/\gamma^* \to \ell\ell$ and W+jets events are normalized to their respective NNLO cross sections [35]. The $t\bar{t}$ sample is normalized by the top pair production cross section measured by CMS [36] times a scale-factor of 1.016, measured in a $t\bar{t}$ enriched control region in the MSSM $H \to \tau\tau$ analysis [37]. Furthermore, a kinematic reweighting, used to better match the top quark p_T distribution observed in data, is applied to simulated $t\bar{t}$ events [38, 39]. The single-top and di-boson events are normalized to their respective NLO cross sections [40].

Standard model single Higgs boson productions are modeled using POWHEG [41]. The following production processes are considered: gluon-gluon fusion (ggH), vector-boson-fusion (qqH), associated production of the Higgs with W and Z bosons (V+Higgs) and associated production with $t\bar{t}$ and $b\bar{b}$ pairs. The samples have been produced assuming a Higgs mass of

$m_{\mathrm{H}} = 125$ GeV and are normalized according to the cross sections given in Ref. [42] for a Higgs boson of this mass. The Higgs decays that have been taken into account in this analysis are $H \to b\bar{b}$ for ZH and WH productions, $H \to \tau\tau$ for VH and ggH production, and both $H \to b\bar{b}$ and $H \to \tau\tau$ for qqH production.

Additional proton-proton interactions happening in coincidence with the generated events are added before detector simulation in order to match the observed distribution of the number of simultaneous interactions per bunch-crossing (pileup). For this purpose, minimum bias events generated with PYTHIA are added to all generated Monte Carlo samples according to the expected pileup profile at the location of the CMS detector. Simulated events are reweighted in order to match the number of pileup interactions expected in data, which is computed based on the instantaneous luminosity and the pp inelastic cross section. All generated events are passed through the full GEANT [43] based simulation of the CMS detector and are reconstructed using the same version of the CMS event reconstruction software as the data.

A special technique, referred to as embedding, is used to model the background arising from $\mathrm{Z}/\gamma^* \to \tau\tau$ Drell-Yan production. Embedded samples are produced by selecting $\mathrm{Z}/\gamma^* \to \mu\mu$ events in data and replacing the reconstructed muons by generator level tau leptons with the same four-vectors as that of the muons. The taus are decayed using TAUOLA. Tau polarization effects are modeled using TAUSPINNER [44]. The GEANT [43] based detector simulation is used to model the detector response to the τ decay products. The visible τ decay products are reconstructed with the particle flow (PF) algorithm [45, 46], and mixed with the remaining particles of the $\mathrm{Z}/\gamma^* \to \mu\mu$ event, after the two muons are removed. Finally, τ_{h} candidates, jets, and E_T^{miss} are reconstructed, the isolation of electrons and muons is computed, and the event is analyzed as if it were data.

The sample of $\mathrm{Z}/\gamma^* \to \mu\mu$ events that is used as input for the production of $\mathrm{Z}/\gamma^* \to \tau\tau$ embedded samples contains contributions of backgrounds, predominantly from $\mathrm{t\bar{t}} \to \mathrm{W^+b\,W^-\bar{b}} \to \mu^+\nu_\mu \mathrm{b}\,\mu^-\bar{\nu}_\mu \mathrm{b}$. While the overall level of these background contributions is small, on the level of one per mille of the $\mathrm{Z}/\gamma^* \to \tau\tau$ embedded sample, the contamination of the embedded samples with $\mathrm{t\bar{t}}$ background becomes relevant in case a subset of events with one or more b-tagged jets is selected. The $\mathrm{t\bar{t}}$ contribution in the embedded samples is corrected for using $\mathrm{t\bar{t}}$ Monte Carlo simulated events that are fed through the embedding procedure in the same way as the data. Further details of correcting the embedding samples for the $\mathrm{t\bar{t}}$ contamination are given in Sec. 6.1. The QCD background is obtained fully from data, as described in Sec. 6.2.

In order to improve the modeling of the data, corrections to Monte Carlo simulated events are applied. These corrections are related to the τ_{h} trigger efficiency, the τ_{h} energy scale, misidentification of electrons or jets as τ_{h}, E_T^{miss} resolution and response, b-tag efficiency and mistag rate, etc. The corrections are described in detail in Ref. [47]. No trigger efficiency corrections are applied in case of embedded samples, as the trigger efficiency measured in data is applied to the embedded samples as event weight (*cf.* Sec. 4).

3 Particle reconstruction and identification

This section describes the methods employed to identify various particles used in this analysis, such as electrons, muons, jets, missing energy, and taus decaying hadronically.

3.1 Electrons and muons

Electrons and muons are used in this analysis solely for the purpose of vetoing events, as described in Sec. 4. We refer to Ref. [47] for a description of the electron and muon identification

criteria and for the computation of their isolation.

3.2 Hadronic tau decays

Hadronic decays of tau leptons are reconstructed by the "hadrons plus strips" (HPS) identification algorithm [48]. The constituents of the jets are analyzed in order to identify individual tau lepton hadronic decay modes. The τ_h candidates used in this analysis are required to be reconstructed in one of the following modes *single hadron*, *hadron plus one strip*, *hadron plus two strips* or *three hadrons*. The presence of extra particles within the jet, not compatible with the reconstructed decay mode of the tau, is used as criterion to discriminate hadronic tau decays from quark and gluon jets. Additional discriminators are provided to separate hadronic tau decays from electrons and muons.

3.3 Jets

Jets within the pseudorapidity $|\eta| < 4.7$ are built using the anti-k_T algorithm [49] with a distance parameter $R = 0.5$, using particles reconstructed by the PF algorithm as input. Reconstructed jets are required to pass two levels of jet identification criteria: fake jets, mainly arising from calorimeter noise, are rejected by requiring reconstructed jets to pass a set of loose jet identification criteria [50]. Jets originating from pileup interactions are suppressed by a jet identification discriminator [51] based on multivariate (MVA) techniques. The energy of reconstructed jets is calibrated as function jet p_T and η [52]. Fastjet-ρ-based [53, 54] jet energy corrections are applied in order to correct for pileup effects.

Calibrated jets of $|\eta| < 2.4$ and $p_T > 20$ GeV that have a discriminator value of the "Combined Secondary Vertex" (CSV) algorithm [55] of $d > 0.679$ are considered b-tagged. The discriminator threshold corresponds to the medium working point (WP) defined in Ref. [55].

3.4 Missing transverse energy

The missing transverse energy, E_T^{miss}, in the event is reconstructed using a MVA based algorithm [56]. This algorithm utilizes the fact that pileup predominantly produces low p_T jets and "unclustered energy" (hadrons not within jets), while leptons and high p_T jets are almost exclusively produced by the hard-scatter interaction, even in high pileup conditions. The two τ candidates reconstructed by the HPS algorithm are considered as "leptons" for the purpose of reconstructing E_T^{miss}. In addition, the algorithm provides event-by-event estimates of the E_T^{miss} resolution. Compared to previously used E_T^{miss} reconstruction algorithms, this MVA based algorithm reduces the sensitivity to pileup significantly and improves the E_T^{miss} resolution by about 40% in pileup conditions typical for the 2012 data-taking period [56].

4 Event selection

In this analysis a combination of a single jet trigger (with a p_T threshold of 320 GeV) and a di-tau trigger (with a p_T threshold of 35 GeV for each tau) was used to select events in data. If the event contained no hadronically decaying tau with p_T greater than 350 GeV, the event is required to have fired the di-tau trigger. Otherwise, it is required to have passed the single jet trigger. A further selection of events consists of a set of generic cuts, which ensure that the data considered in the analysis is of good quality, and a set of analysis specific selection criteria, determined by trigger requirements and the need to suppress specific backgrounds. The generic selection criteria that are applied to events in the signal region as well as to events in the background dominated control regions (described in Sec. 6) require the events to pass a

good-run selection and pass the trigger conditions mentioned above. The events are required to have a primary vertex within $|z_{vtx}| < 24$ cm, $|r| < 2$ cm. The vertex with the highest $\sum p_{\mathrm{T}}$ of associated tracks is selected as the vertex of the hard-scatter interaction in the event.

Special treatment concerning the trigger is needed when processing the $\mathrm{Z}/\gamma^* \to \tau\tau$ embedded samples, due to the fact that the trigger decision used in the analysis is not available in the embedded $\mathrm{Z}/\gamma^* \to \mu\mu$ data which was selected using muon triggers. Instead of requiring the embedded events to pass the trigger requirements, we weight the events by the efficiency for $\mathrm{Z}/\gamma^* \to \tau\tau$ events to pass the trigger conditions. The efficiencies have been measured in data, using the procedure described in Ref. [47].

The following additional selection criteria are applied to events considered in the signal region:

- The event is required to contain two hadronic taus of $p_{\mathrm{T}} > 45$ GeV and $|\eta| < 2.1$, which are reconstructed by the HPS algorithm and pass the tight WP of the MVA-based tau identification discriminator that includes tau lifetime information [57]. In case the p_T of the leading τ_{h} candidate is below 350 GeV and the event is recorded by the di-Tau trigger, both τ_{h} candidates are required to be matched, within $\Delta R < 0.5$, to the tau objects that trigger the event. For events with a leading τ_{h} candidate of $p_T > 350$ GeV, the leading τ_{h} candidate is required to be matched in ΔR to the highest p_T jet that triggers the event. This matching requirement is not applied to reconstructed τ_{h} candidates in case of the embedded samples. It is further required that the τ_{h} with the lower p_{T} of the two passes the loose WP of the MVA-based discriminator against electrons.
- The two τ_{h} candidates are required to be of opposite charge. The di-tau mass, reconstructed by the SVfit algorithm (as described in the following section), is required to be $80 < m_{\tau\tau} < 140$ GeV. In case multiple combinations exist in an event, the combination with the highest sum of raw outputs of the MVA tau identification discriminator is taken.
- The event is required to contain two jets of $p_{\mathrm{T}} > 20$ GeV and $|\eta| < 4.7$. The jets are required to be separated from each of the two τ_{h} candidates by $\Delta R > 0.5$.
- The mass of the two jets is required to be within the window $80 < m_{jj} < 170$ GeV before the kinematic fit is used. The χ^2 of the kinematic fit, which quantifies the level of compatibility of the mass of the jet pair with $m_{\mathrm{H}} = 125$ GeV (*cf.* Sec. 4.1), is required to satisfy $\chi^2 < 20$.
- Events containing an isolated electron of $p_{\mathrm{T}} > 15$ GeV and $|\eta| < 2.4$, passing the cut-based "veto" electron identification criteria or an isolated muon of $p_{\mathrm{T}} > 15$ GeV and $|\eta| < 2.4$, reconstructed as global and as tracker muon and passing the particle-flow muon identification criteria, are rejected. Electrons and muons are considered to be isolated if they satisfy a cut on the relative isolation, $I_\ell < 0.30 \cdot p_{\mathrm{T}}^{\ell}$ (ℓ = e, μ), with I_ℓ computed as described in Ref. [47].

In the non-resonant di-Higgs production, the Higgs are boosted and as a result the tau lepton pair coming from their decays are also boosted. Therefore, in the non-resonant search, the distance in η-ϕ between the two τ_{h} candidates is required to satisfy the condition $\Delta R_{\tau\tau} < 2.0$.

4.1 Di–Higgs mass reconstruction

The Higgs boson that decays into a pair of tau leptons is reconstructed by the SVfit algorithm [58]. The algorithm published in Ref. [58] has been extended to allow for the reconstruction of the full four-momentum vector (p_{T}, η, ϕ, and mass) of the tau lepton pair. No constraint is

applied on the mass of the tau lepton pair.

In case of resonant di-Higgs production, we reconstruct the four-vector of the Higgs boson that decays into bottom quarks by means of a kinematic fit. The fit varies the energy and mass of each b-jet within their expected resolution, subject to the constraint that the mass of the two b-jets equals $m_{\mathrm{H}} = 125$ GeV. The mass of the di-Higgs system, m_{HH}, is then computed by adding the reconstructed four-vectors of the two Higgs bosons.

In case of the non-resonant HH production, an estimator for the mass of the di-Higgs system, referred to as m_{T2} in the literature [59, 60], is used as shape variable to separate the signal from backgrounds. The observable m_{T2} provides an upper kinematic bound on the mass of the di-Higgs system in each event. The variable performs well, in particular, in separating the signal from the large $t\bar{t}$ background. While for signal events m_{T2} extends up to 300-400 GeV, the m_{T2} distribution for $t\bar{t}$ background events is concentrated below the top mass.

5 Definition of event categories

The presence of two b-tagged jets in the final state of HH $\rightarrow$ bb$\tau\tau$ signal events is expected. As the efficiency to reconstruct both b-jets is limited by the b-tagging efficiency of $\approx 36\%$, the efficiency of the signal selection is enhanced by allowing events with one b-tagged jet plus one non-b-tagged jet to contribute to the analysis. A control region containing events with two or more jets, none of which passes the b-tagging criteria, is used to constrain systematic uncertainties. More specifically, the three event categories are:

- **2jet2tag**
  Events in this category are required to contain at least two jets of $p_{\mathrm{T}} > 20$ GeV, $|\eta| < 2.4$ and passing the medium WP ($d > 0.679$) of the CSV b-tag discriminator (*cf.* Sec. 3.3).
- **2jet1tag**
  Events in this category are required to contain one jet of $p_{\mathrm{T}} > 20$ GeV, $|\eta| < 2.4$ and passing the medium WP of the CSV b-tag discriminator plus one or more additional jet of $p_{\mathrm{T}} > 20$ GeV. The additional jet is required to either not satisfy $|\eta| < 2.4$ or to fail the medium WP of the CSV b-tag discriminator.
- **2jet0tag**
  Events in this category are required to contain at least two jets of $p_{\mathrm{T}} > 20$ GeV, all of which either do not satisfy $|\eta| < 2.4$ or fail the medium WP of the CSV b-tag discriminator.

The above mentioned categories are exclusive of one another. For the purpose of studying the modelling of the data by the Monte Carlo simulation in a region that is not sensitive to the presence or absence of a signal, we define as "inclusive" event category the conjunction of the three categories 2jet2tag, 2jet1tag and 2jet0tag. The cuts on $m_{\tau\tau}$, m_{jj}, χ^2, and $\Delta R_{\tau\tau}$ are not applied in the inclusive category.

6 Background estimation

This section describes how contributions from various background channels are estimated. The highest amount of contamination in this analysis comes from QCD events. The next impotant contribution to the background comes from the $\mathrm{Z}/\gamma^* \rightarrow \tau\tau$ decays, followed by the W+jets events.

6.1 $Z/\gamma^* \to \tau\tau$

The dominant irreducible $Z/\gamma^* \to \tau\tau$ background is modeled by applying the embedding method to $Z/\gamma^* \to \mu\mu$ events selected in the $\sqrt{s} = 8$ TeV data as described in Sec. 2. The embedded samples are normalized to the sum of event yields obtained from the $Z/\gamma^* \to \tau\tau$ Monte Carlo sample produced by MADGRAPH plus the $t\bar{t}$ MC embedded sample, in the inclusive event category.

The contamination of the embedded samples with $t\bar{t}$ background is corrected by subtracting the shape and the estimated yield of the $t\bar{t}$ MC embedded from the $Z/\gamma^* \to \tau\tau$ embedded sample. The subtraction is performed separately for each event category. In case the difference of $Z/\gamma^* \to \tau\tau$ embedded minus $t\bar{t}$ MC embedded sample is negative in a given bin, the content of this bin is set to zero. Otherwise the uncertainty on the bin content is set to the sum of uncertainties of $Z/\gamma^* \to \tau\tau$ embedded plus $t\bar{t}$ MC embedded sample in that bin, added in quadrature.

The embedded samples cover only part of the $Z/\gamma^* \to \tau\tau$ background, namely events in which both reconstructed hadronic taus match a $\tau \to \tau_h\nu$ decay on generator level, due to cuts that are applied to the MC generator during the production of the embedded samples. These cuts are applied in the production of the embedded samples, in order to maximize the event statistics of $Z/\gamma^* \to \tau\tau$ background events passing the analysis cuts described in Sec. 4. The small additional contribution arising from $Z/\gamma^* \to \tau\tau$ background events in which one or both reconstructed τ_h are due to a misidentified electron, muon or jet are taken from the $Z/\gamma^* \to \tau\tau$ Monte Carlo sample produced by MADGRAPH.

6.2 QCD

QCD multijet production constitutes the largest reducible background in this analysis. Both reconstructed hadronic tau candidates in these events are typically due to a jet faking the τ_h. The QCD background contribution is determined fully from data, by measuring the probability for the "leading" (higher p_T) τ_h candidate in the event to either pass the tight WP or pass the very loose WP, but fail the tight WP of the MVA-based tau identification discriminator that includes tau lifetime information. The probabilities are measured in events in which both τ_h candidates are of the same charge ("SS" sample). The inclusive event category selection is applied. The measurement is performed as a function of the τ_h candidate p_T in three regions of η: $|\eta| < 1.2$, $1.2 < |\eta| < 1.7$ and $1.7 < |\eta| < 2.1$. The ratio of the probability to pass the tight WP to the probability to pass the very loose WP, but fail the tight WP is denoted by P_{fr}. The probabilities are fitted with linear functions, as a function of the p_T of the τ_h candidate.

The shape template and normalization for the QCD background in the signal region is obtained by selecting events which pass the event and category selection criteria described in Secs. 4 and 5, except that the "leading" τ_h candidate in the event is required to pass the very loose WP, but fail the tight WP. This is referred to as the "OS anti-iso" sample. The probability to pass the tight WP, taken from the linear function that has been fitted to P_{fr}, is applied as an event weight. Contributions of other backgrounds to the SS and OS anti-iso samples are subtracted based on Monte Carlo predictions.

6.3 $t\bar{t}$

The contribution of $t\bar{t}$ background is modeled using the Monte Carlo simulation. The reweighting of simulated $t\bar{t}$ events, described in Sec. 2, is applied in order to improve the agreement between the top-quark p_T spectra in data and Monte Carlo simulation. Measurements of the

differential $t\bar{t}$ production cross section [39] indicate that the kinematics of $t\bar{t}$ are well modeled by the Monte Carlo simulation after this correction is applied.

6.4 W + jets, $Z/\gamma^* \to \ell\ell$, single top and di-boson

The background contributions arising from W+jets, $Z/\gamma^* \to \ell\ell$ (ℓ = e, μ), single top and di-boson production are small and are modeled using the Monte Carlo simulation. Corrections are applied to account for differences between data and Monte Carlo simulation in the jet $\to \tau_h$ and e $\to \tau_h$ misidentification rates, as described in Sec. 2.

7 Systematic uncertainties

We distinguish between yield and shape systematic uncertainties. Yield uncertainties are those which affect the number of signal or background events selected in a given event category and channel. Shape uncertainties are those which affect the number of signal or background events in individual bins of kinematic distributions. Changes in normalization, given by the sum of the signal or background expectation in all bins, may be possible for the shape uncertainties that we consider too. The yield and shape systematics relevant for this analysis are discussed in Secs. 7.1 and 7.2, respectively.

An additional uncertainty arises from limited statistics available to model the m_{HH} and m_{T2} distributions of individual backgrounds in some of the event categories. The treatment of such uncertainties is described in Sec. 8.

7.1 Yield systematics

- **τ_h trigger and identification efficiency**
  The uncertainty on the τ_h identification efficiency been measured using $Z/\gamma^* \to \tau\tau \to \mu\tau_h$ events and amounts to 6% [57]. Hadronic taus in $Z/\gamma^* \to \tau\tau$ events typically have a transverse momenta in the range 20 to 50 GeV. An uncorrelated uncertainty of $20\% \cdot \frac{p_T}{1000\ \mathrm{GeV}}$ is added to account for the extrapolation to high p_T. The uncertainty on the efficiency of the $\tau_h\tau_h$ trigger amounts to 4.5% per leg. The uncertainty in the MC modelling of the trigger ineffiency for high p_T τ_h candidates is also taken into account (*cf.* Ref. [47]). We take 100% of the efficiency drop, parametrized as a function of tau p_T, as the systematic uncertainty.
- **Background yields**
  The rate of the $Z/\gamma^* \to \ell\ell$ (ℓ = e, μ) background is attributed an uncertainty of 5%. The normalization of the $Z/\gamma^* \to \tau\tau$ embedded samples in the inclusive event category, obtained using Monte Carlo samples produced by MADGRAPH as described in Sec. 6.1, is attributed an uncertainty of 5%. An additional uncertainty of 5% is assigned to the fraction of $Z/\gamma^* \to \tau\tau$ events entering the 2jet2tag and 2jet1tag categories. The uncertainty has been introduced by the SM and MSSM H $\to \tau\tau$ analyses [61, 62] to cover potential small biases of the embedding technique described in section 6.1. The uncertainty on the yield of $t\bar{t}$, single top and di-boson backgrounds amounts to 15%. The rate of W+jets background is known with an uncertainty of 30%. These are conservative estimates.
- **Luminosity**
  The uncertainty on the luminosity amounts to 2.6% [63]. This uncertainty is applied to the signal and to $Z/\gamma^* \to \ell\ell$ (ℓ = e, μ, τ), W+jets, single top and di-boson backgrounds. Note that the luminosity uncertainty does not apply to the $t\bar{t}$ background,

as the $t\bar{t}$ background is normalized using a $t\bar{t}$ dominated control region in data (*cf.* Sec. 2). The normalization of the QCD background is obtained from data and hence not subject to the luminosity uncertainty.

7.2 Shape systematics

- τ_h **energy scale**
  The energy scale of hadronically decaying taus is varied by 3%, following CMS recommendation [57].
- **Jet energy scale**
  Jet energy scale uncertainties range from 1-10% and are provided as functions of jet p_T and η [64]. They affect the yield of signal and background events in the different event categories and the shape of the m_{HH} distribution. The jet energy scale uncertainties are not propagated to the E_T^{miss}. The E_T^{miss} related uncertainties on the m_{HH} and m_{T2} distributions are instead covered by the Z-recoil correction uncertainties. The Z-recoil correction is computed by comparing data with MC in $Z \to ee$, $Z \to \mu\mu$, and photon + jets samples, which do not have any intrinsic E_T^{miss}.
- b**-tagging efficiency and mistag rate**
  Uncertainties on b-tagging efficiencies and mistag rates are evaluated as functions of jet p_T and η as recommended in Ref. [55]. The effect of these uncertainties on the analysis is evaluated by varying the Monte Carlo-to-data scale-factors described in Sec. 2 by plus or minus one standard deviation and reanalyzing the events. As the scale-factors depend on p_T and η, the uncertainties on b-tagging efficiencies and mistag rates may affect the shape of the m_{HH} and m_{T2} distributions.
- **QCD background estimation**
  The uncertainty on the normalization and shape of the QCD background is obtained by adding the statistical uncertainty on the yield of events in the OS anti-iso sample in quadrature with the uncertainty on the the slope and offset parameters of the function used to fit P_{fr}, as described in Sec. 6.2.
- E_T^{miss} **resolution and response**
  Uncertainties on E_T^{miss} resolution and response are accounted for by varying the Z-recoil correction parameters within the uncertainties determined within the method. The E_T^{miss} and all E_T^{miss} related observables (including m_{HH} and m_{T2}) are recomputed after each such variation.
- **Top quark** p_T **reweighting**
  The reweighting that is applied to simulated $t\bar{t}$ events (*cf.* Sec. 2) is varied between nominal and twice the nominal correction being applied. [37, 38].

8 Signal extraction

Upper limits on the signal rate are determined by a binned maximum likelihood fit for the *signal plus background* and *background-only* hypotheses. In case of resonant (non-resonant) di-Higgs boson production, we fit the distribution of m_{HH} (m_{T2}), reconstructed as described in Sec. 4.1. We follow a modified frequentist approach, known as the CL_s method [65–67]. Statistical uncertainties on the shape templates are accounted for via the Barlow-Beeston method [68, 69]. Constraints on yield uncertainties are represented by either log-normal or by Gamma probability density functions. Uncertainties which correspond to multiplicative factors on the signal or background yield (e.g. cross sections, efficiencies, fake-rates and sideband extrapolation fac-

tors) are represented by log-normal constraints. Systematic uncertainties that are of statistical origin, e.g. corresponding to the number of events observed in a control region, are represented by Gamma distributions. Systematic uncertainties in the shape of the m_{HH} and m_{T2} distribution for signal as well as background processes are accounted for by the "vertical template morphing" technique [69]. A bias that is introduced due to the limited event statistics in the m_{HH} and m_{T2} shape templates is taken into account by the Barlow-Beeston method [68, 69].

In order to make the signal extraction less demanding in terms of computing time, the number of nuisance parameters representing statistical fluctuations of the shape templates are reduced by summing the statistical uncertainties of all backgrounds contributing to a given bin in quadrature and attributing the combined uncertainty to the dominant background. Statistical uncertainties which are within 10% of the background contribution expected in a given bin are neglected.

9 Results

9.1 Observed yields

The number of events observed in the 2jet2tag, 2jet1tag, and 2jet0tag categories as well as the expected yield of background processes are given in Tab. 1.

The distribution of m_{HH} (m_{T2}) for the events selected in the 2jet2tag, 2jet1tag, and 2jet0tag category in case of the resonant (non-resonant) analysis are shown in Figs. 3 and 4. The event yields and mass distributions observed in data are in agreement with the background prediction. No evidence for the presence of a signal is observed.

9.2 Cross section limits

In the absence of evidence for a signal, we proceed by setting 95% CL upper limits on cross section times branching ratio for the production of resonances decaying to a pair of SM-like Higgs bosons of mass $m_{\mathrm{H}} = 125$ GeV and on non-resonant di-Higgs boson production. The difference between the limits computed for radion $\rightarrow$ HH and graviton $\rightarrow$ HH signals is small, indicating that the limits on resonant di-Higgs boson production do not depend on these particular models. In case of non-resonant HH production, the limit has been computed assuming SM event kinematics. Some model dependency is expected in this case, as the signal acceptance times efficiency as well as the shape of the m_{T2} distribution vary as functions of the m_{HH} spectrum predicted by the model. The limits obtained for resonant di-Higgs boson production are given in Tab. 2 and are shown in Fig. 5. In this figure, the expected limits were computed for a generic Spin-0/2 resonance decaying to 2 SM Higgs bosons. The theory curves for the graviton case were based on KK graviton production in the bulk and RS1 models, respectively [70, 71]. To obtain the radion theory curves, cross section for radion production via gluon fusion were computed (to NLO electroweak and NNLO QCD accuracy) for different values of fundamental theory parameter Λ_R which were then multplied by a K-factor calculated for SM-like Higgs boson production through gluon-gluon fusion [72–74]. For non-resonant HH production the observed (expected) limits on $\sigma(\mathrm{pp} \rightarrow \mathrm{HH})$ amounts to 0.59 pb ($0.94\ ^{+0.46}_{-0.24}$ pb), corresponding to 53 (84) times the cross section predicted by the SM.

A search for non-resonant and resonant di-Higgs boson production has been performed by the ATLAS collaboration in the $b\bar{b}\tau\tau$, $\gamma\gamma WW^*$, $\gamma\gamma b\bar{b}$, and $b\bar{b}b\bar{b}$ channels [27]. The observed (expected) limit for non-resonant di-Higgs boson production, obtained from the combination of all channels, amounts to 70 (48) times the SM cross section. In the bbtautau channel alone, a

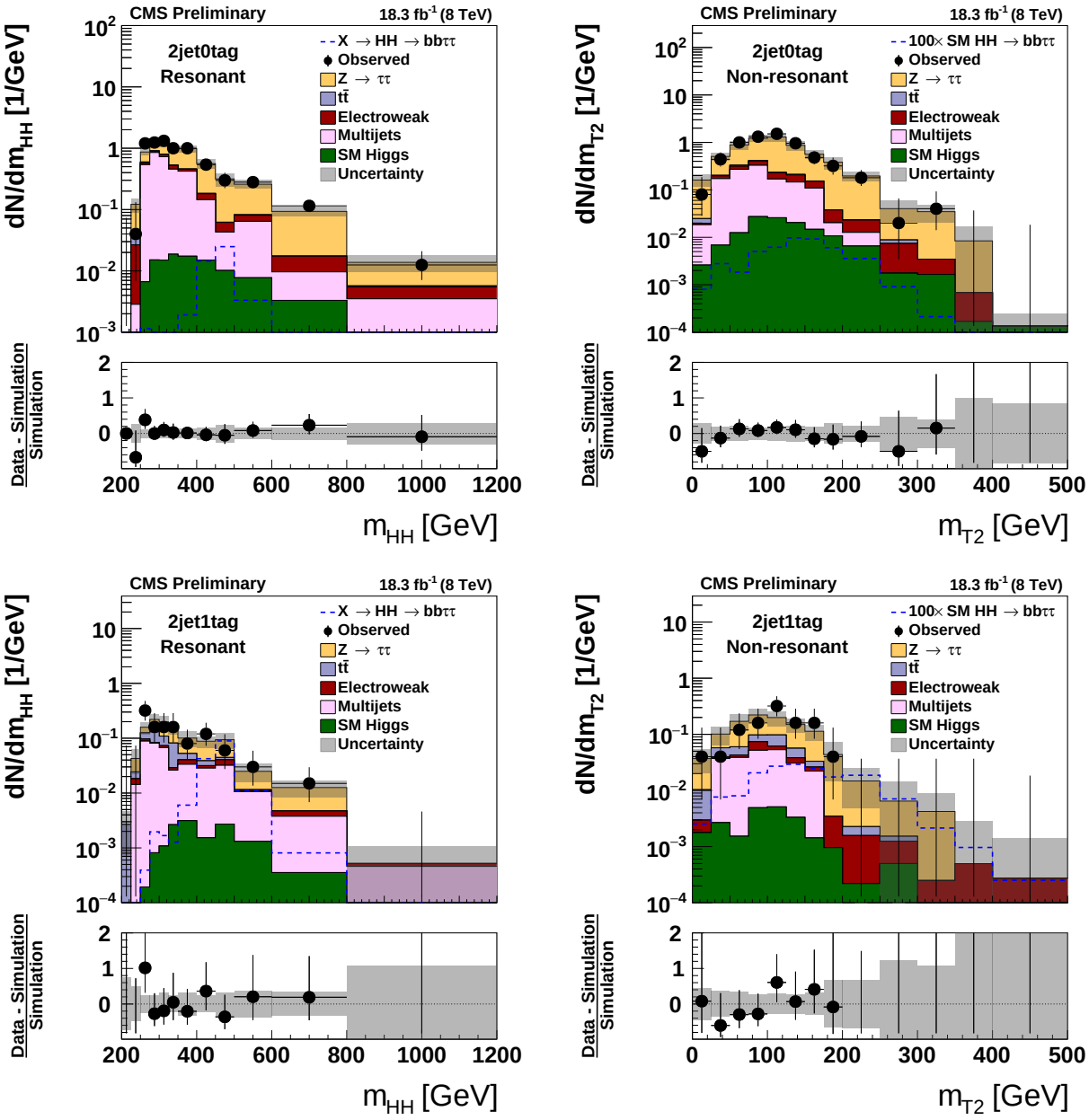

Figure 3: Distribution of m_{HH} (left) and of m_{T2} (right) observed in the 2jet0tag (top) and 2jet1tag (bottom) event category, compared to the expectation for background processes. Hypothetical signals have been overlayed for comparison. The signal shown in case of the m_{HH} distribution corresponds to the decays of a spin 2 resonance X of mass $m_X = 500$ GeV that is produced with a cross section times branching fraction of $\sigma(\mathrm{pp} \to X) \times \mathrm{BR}(X \to \mathrm{HH}) = 1$ pb. In case of the m_{T2} distribution, a non-resonant HH signal with a cross section $\sigma(\mathrm{pp} \to \mathrm{HH})$ of 1.118 pb, corresponding to 100 times the SM cross section, is shown. The expectation for signal and background processes is shown for the *postfit* values of nuisance parameters.

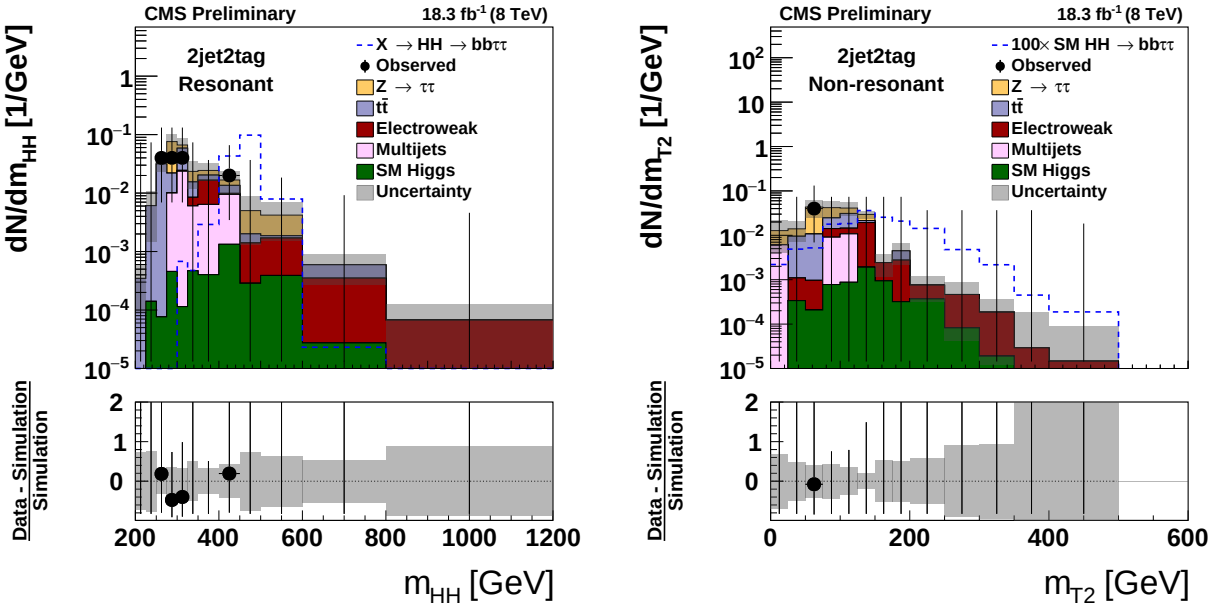

Figure 4: Distribution of m_{HH} (left) and of m_{T2} (right) observed in the 2jet2tag event category, compared to the expectation for background processes. Hypothetical signals have been overlayed for comparison. The signal shown in case of the m_{HH} distribution corresponds to the decays of a spin 2 resonance X of mass $m_X = 500$ GeV that is produced with a cross section times branching fraction of $\sigma(\mathrm{pp} \to X) \times \mathrm{BR}(X \to \mathrm{HH}) = 1$ pb. In case of the m_{T2} distribution, a non-resonant HH signal with a cross section $\sigma(\mathrm{pp} \to \mathrm{HH})$ of 1.118 pb, corresponding to 100 times the SM cross section, is shown. The expectation for signal and background processes is shown for the *postfit* values of nuisance parameters.

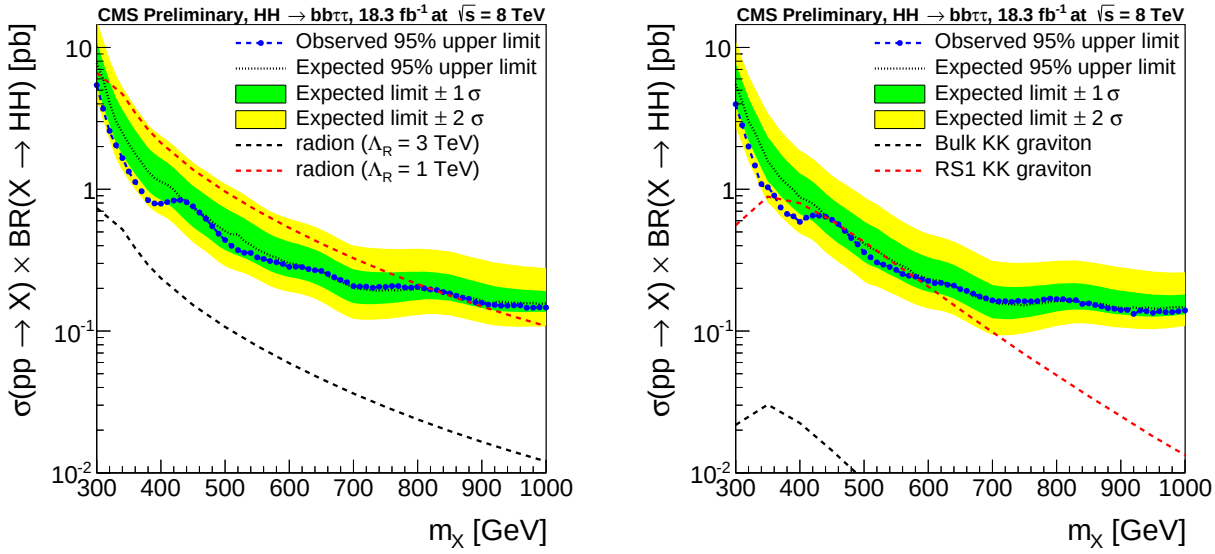

Figure 5: 95% CL upper limits on resonant HH production. The limits for resonant di-Higgs boson production have been computed for a spin 0 (left) and for a spin 2 (right) resonance X and are shown as function of the resonance mass m_X. The theory curves for the graviton case were based on KK graviton production in the bulk and RS1 models respectively [70, 71]. To obtain the radion theory curves, cross section for radion production via gluon fusion were computed (to NLO electroweak and NNLO QCD accuracy) for different values of fundamental theory parameter Λ_R which were then multplied by a K-factor calculated for SM-like Higgs boson production through gluon-gluon fusion [72–74].

Non-resonant analysis			
Process	2jet0tag	2jet1tag	2jet2tag
Non-resonant HH production	1.3 ± 0.2	5.1 ± 0.7	4.7 ± 0.6
$Z \to \tau\tau$	120.3 ± 11.1	17.7 ± 3.0	2.0 ± 0.8
QCD multijet	27.9 ± 2.7	5.4 ± 1.0	0.7 ± 0.2
W+jets	4.3 ± 0.8	0.4 ± 0.1	0.4 ± 0.1
Z+jets (e, μ or jet faking τ_h)	0.7 ± 0.2	< 0.1	< 0.1
$t\bar{t}$	1.3 ± 0.2	3.4 ± 0.5	1.2 ± 0.2
Di-bosons + single top	5.7 ± 1.0	1.1 ± 0.2	0.5 ± 0.1
SM Higgs	3.7 ± 1.3	0.6 ± 0.2	0.2 ± 0.1
Total expected	163.9 ± 11.4	28.6 ± 3.2	5.2 ± 1.1
Observed data	165	26	1

Resonant analysis			
Process	2jet0tag	2jet1tag	2jet2tag
Radion $\to$ HH	1.6 ± 0.2	5.7 ± 0.7	6.2 ± 0.8
Graviton $\to$ HH	2.4 ± 0.3	7.8 ± 0.9	7.6 ± 0.9
$Z \to \tau\tau$	130.6 ± 13.8	19.8 ± 3.4	2.7 ± 1.0
QCD multijet	92.7 ± 8.1	12.6 ± 2.2	1.8 ± 0.6
W+jets	8.4 ± 1.5	0.8 ± 0.3	0.4 ± 0.1
Z+jets (e, μ or jet faking τ_h)	1.6 ± 0.5	< 0.1	0.2 ± 0.1
$t\bar{t}$	2.5 ± 0.4	5.2 ± 0.7	2.7 ± 0.5
Di-bosons + single top	6.1 ± 1.1	1.7 ± 0.4	0.5 ± 0.1
SM Higgs	5.0 ± 1.7	0.7 ± 0.2	0.2 ± 0.1
Total expected	246.8 ± 13.9	40.6 ± 3.9	8.4 ± 1.3
Observed data	268	39	4

Table 1: Observed and expected event yields in different event categories, for the analysis of non-resonant (top) and resonant (bottom) HH production. Expected event yields are computed using values of nuisance parameters obtained by the maximum likelihood fit to the data as described in Sec. 8. Quoted uncertainties represent the combination of statistical plus systematic uncertainties. In case of resonant di-Higgs boson production, the signal yield has been computed for a resonance with of mass $m_X = 500$ GeV and a radion or graviton production cross section times branching fraction of $\sigma(pp \to X) \times BR(X \to HH) = 1$ pb. The signal rate expected for non-resonant HH production has been computed for a cross section $\sigma(pp \to HH)$ of 1.118 pb, corresponding to 100 times the SM cross section, and SM event kinematics.

limit of 160 (130) times the SM cross section is observed (expected). For the production of a resonance X of mass $m_X = 500$ GeV that decays into a pair of H bosons, the ATLAS collaboration sets an observed (expected) limit of 0.61 pb (0.38 pb) from the combination of all channels, and a limit of 1.0 pb (0.66 pb) is observed (expected) in the bbtautau channel alone.

10 Summary

A search for events containing a pair of SM-like Higgs bosons of mass $m_H = 125$ GeV has been performed. Resonant as well as non-resonant production of the Higgs boson pair has been studied in the channel where one Higgs boson decays to a pair of b-quarks and the other Higgs boson decays to a tau lepton pair, using pp collision data recorded by the CMS experiment at 8 TeV center-of-mass energy in 2012, corresponding to an integrated luminosity of 18.3 fb^{-1}.

m_X	Radion ($J = 0$)		Graviton ($J = 2$)	
[GeV]	Expected	Observed	Expected	Observed
300	7.78	5.42	5.51	3.97
350	2.08	1.33	1.58	1.03
400	1.13	0.79	0.87	0.58
450	0.73	0.75	0.61	0.60
500	0.50	0.44	0.41	0.36
600	0.30	0.28	0.23	0.23
700	0.20	0.21	0.16	0.16
800	0.19	0.20	0.16	0.16
900	0.16	0.16	0.14	0.14
1000	0.15	0.14	0.14	0.14

Table 2: 95% CL upper limits on resonant HH production in units of pb for spin $J = 0$ (radion) and spin $J = 2$ (graviton) resonances X, at different masses m_X.

No evidence for a signal is observed and corresponding upper limits on the signal rate are set. In case of resonant HH production, the limit on $\sigma(\mathrm{pp} \to X) \times \mathrm{BR}(X \to \mathrm{HH})$ for a resonance of spin 0 (spin 2) of mass m_X ranges from 5.42 pb (3.97 pb) at $m_X = 300$ GeV to 0.14 pb (0.14 pb) at $m_X = 1000$ GeV. The limit on non-resonant production amounts to 53 times the rate predicted by the SM. This limit has been computed assuming SM event kinematics.

References

[1] CMS Collaboration, "Observation of a new boson at a mass of 125 GeV with the CMS experiment at the LHC", *Phys. Lett.* **B716** (2012) 30–61, doi:10.1016/j.physletb.2012.08.021, arXiv:hep-ex/1207.7235.

[2] ATLAS Collaboration, "Observation of a new particle in the search for the Standard Model Higgs boson with the ATLAS detector at the LHC", *Phys. Lett.* **B716** (2012) 1–29, doi:10.1016/j.physletb.2012.08.020, arXiv:hep-ex/1207.7214.

[3] Particle Data Group Collaboration, "Review of Particle Physics", *Chin. Phys.* **C38** (2014) 090001, doi:10.1088/1674-1137/38/9/090001.

[4] T. Plehn and M. Rauch, "The quartic higgs coupling at hadron colliders", *Phys. Rev.* **D72** (2005) 053008, doi:10.1103/PhysRevD.72.053008, arXiv:hep-ph/0507321.

[5] U. Baur, T. Plehn, and D. L. Rainwater, "Determining the Higgs boson selfcoupling at hadron colliders", *Phys. Rev.* **D67** (2003) 033003, doi:10.1103/PhysRevD.67.033003, arXiv:hep-ph/0211224.

[6] U. Baur, T. Plehn, and D. L. Rainwater, "Probing the Higgs selfcoupling at hadron colliders using rare decays", *Phys. Rev.* **D69** (2004) 053004, doi:10.1103/PhysRevD.69.053004, arXiv:hep-ph/0310056.

[7] M. J. Dolan, C. Englert, and M. Spannowsky, "Higgs self-coupling measurements at the LHC", *JHEP* **10** (2012) 112, doi:10.1007/JHEP10(2012)112, arXiv:hep-ph/1206.5001.

[8] F. Goertz, A. Papaefstathiou, L. L. Yang, and J. Zurita, "Higgs Boson self-coupling measurements using ratios of cross sections", *JHEP* **06** (2013) 016, doi:10.1007/JHEP06(2013)016, arXiv:hep-ph/1301.3492.

[9] D. de Florian and J. Mazzitelli, "Higgs pair production at next-to-next-to-leading logarithmic accuracy at the LHC", *JHEP* **09** (2015) 053, doi:10.1007/JHEP09(2015)053, arXiv:hep.ph/1505.07122.

[10] J. Butterworth et al., "PDF4LHC recommendations for LHC Run II", *J. Phys. G* **43** (2016) 023001, doi:10.1088/0954-3899/43/2/023001, arXiv:hep-ph/1510.03865.

[11] LHC Higgs Cross Section Working Group. https://twiki.cern.ch/twiki/bin/view/LHCPhysics/LHCHXSWGHH.

[12] N. Craig, J. Galloway, and S. Thomas, "Searching for Signs of the Second Higgs Doublet", arXiv:hep-ph/1305.2424.

[13] D. T. Nhung, M. Muhlleitner, J. Streicher, and K. Walz, "Higher Order Corrections to the Trilinear Higgs Self-Couplings in the Real NMSSM", *JHEP* **11** (2013) 181, doi:10.1007/JHEP11(2013)181, arXiv:hep-ph/1306.3926.

[14] R. Grober and M. Muhlleitner, "Composite Higgs Boson Pair Production at the LHC", *JHEP* **06** (2011) 020, doi:10.1007/JHEP06(2011)020, arXiv:hep-ph/1012.1562.

[15] R. Contino et al., "Strong Double Higgs Production at the LHC", *JHEP* **05** (2010) 089, doi:10.1007/JHEP05(2010)089, arXiv:hep-ph/1002.1011.

[16] C. Englert, T. Plehn, D. Zerwas, and P. M. Zerwas, "Exploring the Higgs portal", *Phys. Lett.* **B703** (2011) 298–305, doi:10.1016/j.physletb.2011.08.002, arXiv:hep-ph/1106.3097.

[17] J. M. No and M. Ramsey-Musolf, "Probing the Higgs Portal at the LHC Through Resonant di-Higgs Production", *Phys. Rev.* **D89** (2014) 095031, doi:10.1103/PhysRevD.89.095031, arXiv:hep-ph/1310.6035.

[18] L. Randall and R. Sundrum, "A Large mass hierarchy from a small extra dimension", *Phys. Rev. Lett.* **83** (1999) 3370–3373, doi:10.1103/PhysRevLett.83.3370, arXiv:hep-ph/9905221.

[19] K. Cheung, "Phenomenology of radion in Randall-Sundrum scenario", *Phys. Rev.* **D63** (2001) 056007, doi:10.1103/PhysRevD.63.056007, arXiv:hep-ph/0009232.

[20] W. M. B. Goldberger W. D., "Modulus stabilization with bulk fields", *Phys. Rev. Lett.* **83** (1999) 4922–4925, doi:10.1103/PhysRevLett.83.4922, arXiv:hep-ph/9907447.

[21] F. D. DeWolfe O., "Modeling the fifth-dimension with scalars and gravity", *Phys. Rev.* **D62** (2000) 046008, doi:10.1103/PhysRevD.62.046008, arXiv:hep-ph/9909134.

[22] R. L. Csaki C., Graesser M., "Cosmology of brane models with radion stabilization", *Phys. Rev.* **D62** (2000) 046015, doi:10.1103/PhysRevD.62.046015, arXiv:hep-ph/9911406.

[23] R. T. Davoudiasl H., Hewett J., "Phenomenology of the Randall-Sundrum Gauge Hierarchy Model", *Phys. Rev. Lett.* **84** (2000) 2080, doi:10.1103/PhysRevLett.84.2080, arXiv:hep-ph/9909255.

[24] K. G. D. Csaki C., Graesser M. L., "Radion dynamics and electroweak physics", *Phys. Rev.* **D63** (2001) 065002, doi:10.1103/PhysRevD.63.065002, arXiv:hep-ph/0008151.

[25] ATLAS Collaboration, "Search For Higgs Boson Pair Production in the $\gamma\gamma b\bar{b}$ Final State using pp Collision Data at $\sqrt{s} = 8$ TeV from the ATLAS Detector", *Phys. Rev. Lett.* **114** (2015) 081802, doi:10.1103/PhysRevLett.114.081802, arXiv:hep-ex/1406.5053.

[26] ATLAS Collaboration, "Search For Higgs Boson Pair Production in the $b\bar{b}b\bar{b}$ Final State from pp Collisions at $\sqrt{s} = 8$ TeV from the ATLAS Detector", *Eur. Phys. J.* **C75** (2015) 412, doi:10.1140/epjc/s10052-015-3628-x, arXiv:hep-ex/1506.00285.

[27] ATLAS Collaboration, "Searches for Higgs Boson pair production in the $b\bar{b}\tau\tau$, $\gamma\gamma WW^*$, $\gamma\gamma b\bar{b}$, and $b\bar{b}b\bar{b}$ channels with the ATLAS Detector", arXiv:hep-ex/1506.04670.

[28] CMS Collaboration, "Searches for heavy Higgs bosons in two-Higgs-doublet models and for $t \to ch$ decay using multilepton and diphoton final states in pp collisions at 8 TeV", *Phys. Rev.* **D90** (2014) 112013, doi:10.1103/PhysRevD.90.112013, arXiv:hep-ex/1410.2751.

[29] CMS Collaboration, "Search for resonant pair production of Higgs bosons decaying to two bottom quark-antiquark pairs in pp collisions at 8 TeV", arXiv:hep-ex/1503.04114.

[30] CMS Collaboration, "Searches for a heavy scalar boson H decaying to a pair of 125 GeV Higgs bosons hh or for a heavy pseudoscalar boson A decaying to Zh, in the final states with $h \to \tau\tau$ ", arXiv:hep-ex/1510.01181.

[31] F. Maltoni and T. Stelzer, "MadEvent: Automatic event generation with MadGraph", *JHEP* **02** (2003) 027, arXiv:hep-ph/0208.0156.

[32] A. Read, "Confidence level computation for combining searches with small statistics", *Nucl. Instrum. Meth.* **A357** (1999) 425.

[33] S. M. T. Sjöstrand and P. Skands, "PYTHIA 6.4 Physics and Manual", 2000.

[34] S. Jadach, Z. Was, R. Decker, and J. H. Kuhn, "The Tau Decay Library Tauola: Version 2.4", *Comput. Phys. Commun.* **76** (1993) 361.

[35] K. Melnikov and F. Petriello, "Electroweak gauge boson production at hadron colliders through O(alpha(s)**2)", *Phys. Rev.* **D74** (2006) 114017, doi:10.1103/PhysRevD.74.114017, arXiv:hep-ph/0609070.

[36] CMS Collaboration, "Combination of ATLAS and CMS top quark pair cross section measurements in the eμ final state using proton-proton collisions at $\sqrt{s} = 8$ TeV", *CMS PAS* **TOP-14-016** (2014).

[37] CMS Collaboration, "Measurement of differential top-quark pair production cross section in the dilepton channel in pp collisions at $\sqrt{s} = 8$ TeV", *CMS PAS* **TOP-12-028** (2012).

[38] CMS Collaboration, "Measurement of differential top-quark pair production cross sections in pp colisions at $\sqrt{s} = 7$ TeV", *Eur. Phys. J.* **C 73** (2013) 2339, doi:10.1140/epjc/s10052-013-2339-4, arXiv:1211.2220.

[39] CMS Collaboration, "Measurement of the differential cross section for top quark pair production in pp collisions at $\sqrt{s} = 8$ TeV", (2015). arXiv:hep-ex/1505.04480.

[40] J. M. Campbell, R. K. Ellis, and C. Williams, "Vector boson pair production at the LHC", *JHEP* **07** (2011) 018, doi:10.1007/JHEP07(2011)018, arXiv:1105.0020.

[41] S. Frixione, P. Nason, and C. Oleari, "Matching NLO QCD computations with Parton Shower simulations: the POWHEG method", *JHEP* **11** (2007) 070, arXiv:hep-ph/0709.2092.

[42] LHC Higgs Cross Section Working Group, "Handbook of LHC Higgs Cross Sections: 1. Inclusive Observables", CERN Report CERN-2011-002, 2011. arXiv:hep-ph/1101.0593.

[43] S. Agostinelli et al., "G4–a simulation toolkit", *Nuclear Instruments and Methods in Physics Research Section A: Accelerators, Spectrometers, Detectors and Associated Equipment* **506** (2003), no. 3, 250 – 303, doi:10.1016/S0168-9002(03)01368-8.

[44] Z. Czyczula, T. Przedzinski, and Z. Was, "TauSpinner Program for Studies on Spin Effect in tau Production at the LHC", *EPJC* **72** (2012) 1988, arXiv:hep-ph/1201.0117.

[45] CMS Collaboration, "Particle-Flow Event Reconstruction in CMS and Performance for Jets, Taus, and Missing E_{T}", *CMS PAS* **PFT-09-001** (2009).

[46] CMS Collaboration, "Commissioning of the particle-flow event reconstruction with the first LHC collisions recorded in the CMS detector", *CMS PAS* **PFT-10-001** (2010).

[47] CMS Collaboration, "Search for additional neutral Higgs bosons decaying to a pair of tau leptons in pp collisions at $\sqrt{s} = 7$ and 8 TeV", *CMS PAS* **HIG-14-029** (2014).

[48] CMS Collaboration, "Performance of tau-lepton reconstruction and identification in CMS", *JINST* **7** (2012) P01001, doi:10.1088/1748-0221/7/01/P01001, arXiv:hep-ex/1109.6034.

[49] M. Cacciari, G. P. Salam, and G. Soyez, "The anti-kt jet clustering algorithm", *JHEP* **04** (2008) 063, arXiv:hep-ph/0802.1189.

[50] CMS Collaboration, "Jet performance in pp Collisions at $\sqrt{s} = 7$ TeV", *CMS PAS* **JME-10-003** (2010).

[51] CMS Collaboration, "Pileup Jet Identification", *CMS PAS* **JME-13-005** (2010).

[52] CMS Collaboration, "Determination of Jet Energy Calibration and Transverse Momentum Resolution in CMS", *JINST* **6** (2011) P11002, doi:10.1088/1748-0221/6/11/P11002, arXiv:hep-ex/1107.4277.

[53] M. Cacciari, G. P. Salam, and G. Soyez, "The Catchment Area of Jets", *JHEP* **04** (2008) 005, doi:10.1088/1126-6708/2008/04/005, arXiv:hep-ph/0802.1188.

[54] M. Cacciari and G. P. Salam, "Pileup subtraction using jet areas", *Phys. Lett.* **B659** (2008) 119–126, doi:10.1016/j.physletb.2007.09.077, arXiv:hep-ph/0707.1378.

[55] CMS Collaboration, "Identification of b-quark jets with the CMS experiment", *JINST* **8** (2013) P04013, doi:10.1088/1748-0221/8/04/P04013, arXiv:hep-ex/1211.4462.

[56] CMS Collaboration, "Performance of the CMS missing transverse momentum reconstruction in pp data at $\sqrt{s} = 8$ TeV", *JINST* **10** (2015), no. 02, P02006, doi:10.1088/1748-0221/10/02/P02006, arXiv:physics.ins-det/1411.0511.

[57] CMS Collaboration, "Reconstruction and identification of τ lepton decays to hadrons and ν_τ at CMS", arXiv:hep-ex/1510.07488.

[58] L. Bianchini, J. Conway, E. K. Friis, and C. Veelken, "Reconstruction of the Higgs mass in $H \to \tau\tau$ Events by Dynamical Likelihood techniques", *J.Phys.Conf.Ser.* **513** (2014) 022035, doi:10.1088/1742-6596/513/2/022035.

[59] C. Lester and D. Summers, "Measuring masses of semiinvisibly decaying particles pair produced at hadron colliders", *Phys. Lett.* **B463** (1999) 99–103, doi:10.1016/S0370-2693(99)00945-4, arXiv:hep-ph/9906349.

[60] A. J. Barr, M. J. Dolan, C. Englert, and M. Spannowsky, "Di-Higgs final states augMT2ed – selecting *hh* events at the high luminosity LHC", *Phys. Lett.* **B728** (2014) 308–313, doi:10.1016/j.physletb.2013.12.011, arXiv:hep-ph/1309.6318.

[61] CMS Collaboration Collaboration, "Evidence for the 125 GeV Higgs boson decaying to a pair of τ leptons", *JHEP* **05** (2014) 104, doi:10.1007/JHEP05(2014)104, arXiv:hep-ex/1401.5041.

[62] CMS Collaboration, "Search for neutral MSSM Higgs bosons decaying to a pair of tau leptons in pp collisions", *JHEP* **10** (2014) 160, doi:10.1007/JHEP10(2014)160, arXiv:hep-ex/1408.3316.

[63] CMS Collaboration, "CMS Luminosity Based on Pixel Cluster Counting - Summer 2013 Update", *CMS PAS* **LUM-13-001** (2013).

[64] CMS Collaboration, "Determination of Jet Energy Calibration and Transverse Momentum Resolution in CMS", *JINST* **6** (2011) P11002, doi:10.1088/1748-0221/6/11/P11002, arXiv:physics.ins-det/1107.4277.

[65] A. L. Read, "Presentation of search results: The CL(s) technique", *J.Phys.* **G28** (2002) 2693–2704, doi:10.1088/0954-3899/28/10/313.

[66] ATLAS Collaboration, CMS Collaboration and LHC Higgs Combination Group, "Procedure for the LHC Higgs boson search combination in summer 2011", Technical Report ATL-PHYS-PUB-2011-011, CMS-NOTE-2011-005, 2011.

[67] CMS Collaboration, "Combined results of searches for the standard model Higgs boson in pp collisions at $\sqrt{s} = 7$ TeV", *Phys. Lett.* **B 710** (2012) 26, doi:10.1016/j.physletb.2012.02.064, arXiv:hep-ex/1202.1488.

[68] R. Barlow and C. Beeston, "Fitting using finite Monte Carlo samples", *Computer Physics Communications* **77** (1993) 219–228.

[69] J. S. Conway, "Incorporating Nuisance Parameters in Likelihoods for Multisource Spectra", (2011). arXiv:hep-ex/1103.0354.

[70] O. A. e. a. K. Agashe, "Warped Extra Dimensional Benchmarks for Snowmass 2013., in Community Summer Study 2013: Snowmass on the Mississippi (CSS2013) Minneapolis, MN, USA", arXiv:hep-ph/1309.7847.

[71] P. de Aquino et al., "Simulating graviton production at hadron colliders", *JHEP* **06** (2011) 132, arXiv:hep-ph/1101.5499.

[72] J. D. W. G. F. Giudice, R. Rattazzi, "Graviscalars from higher-dimensional metrics and curvature-Higgs mixing", *Nucl. Phys.* **B595** (2001) 250, arXiv:hep-ph/0002178.

[73] U. Mahanta and A. Datta, "Search prospects of light stabilized radions at Tevatron and LHC", *Phys. Lett.* **B483** (2000) 196, arXiv:hep-ph/0002183.

[74] T. G. R. H. Davoudiasl, J. L. Hewett, "Experimental probes of localized gravity:On and off the wall", *Phys. Rev.* **D63** (2001) 075004, arXiv:hep-ph/0006041.